Chemical and Biochemical Engineering Faculty Research & Creative Works

Linda and Bipin Doshi Department of Chemical and Biochemical Engineering

01 Feb 2016

Characterization of Silica-Based and Borate-Based, Titanium-Containing Bioactive Glasses for Coating Metallic Implants

Omar Rodriguez

Declan J. Curran

Marcello Papini

Lana M. Placek

et. al. For a complete list of authors, see https://scholarsmine.mst.edu/che_bioeng_facwork/1114

CrossMark

Characterization of silica-based and borate-based, titanium-containing bioactive glasses for coating metallic implants

Omar Rodriguez [a,b], Declan J. Curran [a,b], Marcello Papini [a], Lana M. Placek [c], Anthony W. Wren [c], Emil H. Schemitsch [b], Paul Zalzal [d], Mark R. Towler [a,b,e,*]

[a] Department of Mechanical & Industrial Engineering, Ryerson University, Toronto M5B 2K3 Ontario, Canada
[b] St. Michael's Hospital, Toronto M5B 1W8 Ontario, Canada
[c] Inamori School of Engineering, Alfred University, Alfred, NY 14802, USA
[d] Oakville Trafalgar Memorial Hospital, Oakville L6J 3L7 Ontario, Canada
[e] Department of Biomedical Engineering, University of Malaya, Kuala Lumpur, Malaysia

ABSTRACT

Bioactive glasses have found applications in diverse fields, including orthopedics and dentistry, where they have been utilized for the fixation of bone and teeth and as scaffolds for drug delivery. The present work outlines the characterization of two novel titanium-containing glass series, one silica-based and one borate-based. For the silica-based series, titanium is added at the expense of silicon dioxide whereas for the borate-based series, it is added at the expense of boron oxide as confirmed by Energy Dispersive Spectroscopy. Amorphous structures are obtained for silica-based glass at 15 mol% TiO_2 and for borate-based glasses at 0 mol% and 5 mol%, with low crystal peak intensities exhibited within the remaining glasses. MAS-NMR proves the role of P_2O_5 as a network modifier for both glass series by evidencing only Q^0 structures (and Q^1 structures for the silica-based glasses with crystal structures), whereas FTIR proves that Ti acted as a network modifier in the glass as there was an absence of peaks assignable to titanium bonding. This implies that the two glass series will degrade *in-situ* and release ions at the site of implantation. Additionally, thermal data sourced from these glasses indicate processing windows which make them suitable for enameling onto implants, with the borate-based series exhibiting greater processing windows over the silica-based series, hence making the borate glasses more suitable for coating metallic implants compared to their silica-based counterparts.

© 2015 Elsevier B.V. All rights reserved.

1. Introduction

In the field of prosthetics, two technologies for attaching the residual limb and the prosthetic implant are widely utilized: socket attachment and direct skeletal (or bone-anchored) attachment [1]. Socket attachment is the most common method [2], with designs already established for the different applications, *e.g.* below, through or above-knee amputations [3–6]. In general, socket attachment consists of wrapping the prosthetic limb around the residual limb, where the prosthesis serves as the socket for the residual limb, with quadrilateral and ischial containment sockets being the most noteworthy technologies [7]. Compared to socket attachment, direct skeletal attachment (DSA) is a relatively new technology, where an implant is attached directly to the patient's bone at the residual limb. Upon healing, the implant in DSA serves as the attachment mechanism between the prosthesis and the body [1]. In achieving osseointegration, the implant is permanently connected to the bone, resulting in high force and moment interaction between the prosthesis and the body [8]. DSA technology offers the advantage over socket technology *via* a reduction in skin-related complications and residual limb constraints within the socket, which is due to the limited direct contact between the prosthetic implant and the skin [9].

Titanium is regularly used in prosthetics due to its ability to create a permanent bond to bone, *via* osseointegration [10,11], a condition achieved when there is no relative motion between the implant and the bone with which it is in direct contact [12]. It is this characteristic that has also made DSA devices more favorable than socket attachment for prosthetics. Nonetheless, there are concerns regarding DSA that include potential infection, skin irritation and breakdown, implant failure and risk of a broken bone in the residual limb [13–17]. Addressing these concerns will aid in shifting the current paradigm from socket attachment towards DSA.

It is important to understand the overall mechanics of the DSA system, as loads that may negatively affect the residual limb bone may occur in this situation [17]. This places the patients at risk of requiring additional treatment if the bone weakens or fractures due to incomplete osseointegration or due to detrimental bone remodeling induced by

---

* Corresponding author at: Department of Mechanical and Industrial Engineering, Faculty of Engineering and Architectural Science, 350 Victoria Street, Toronto, Ontario, Canada M5B 2K3.

E-mail address: mtowler@ryerson.ca (M.R. Towler).

stress shielding [18]. Different approaches have been taken towards improving the patient's experience with regards to DSA, including modifying the implant surface by chemical etching with hydrochloric and sulfuric acid, sandblasting, titanium plasma-spraying, hydroxylapatite (HA) plasma-spraying, coating the implant with a titanium dioxide (TiO_2) layer through anodic oxidation, and with bioactive glass [9,19–21]. Among these methods, HA coating has been used for over 20 years, exploiting its ability to promote bone ingrowth [22–24]; yet there are concerns with HA use as it has no mechanism to retard bacterial or biofilm colonization at the implant site. Coatings have also been produced based on chlorhexidine and silicone with ammonia couplings [25,26], but these have little clinical applicability due to erosion of the compounds as they migrate to the surface. Of these approaches, bioactive glasses have showed encouraging results [19].

The use of bioactive materials has proliferated since the development of Hench's 45S5 Bioglass® in the 1960s [27] due to its favorable interaction with living tissue. Bioglass was the first synthetic to chemically adhere to both hard and soft tissue [27]. While Hench acknowledged that Bioglass® is unsuitable as a coating [28], he developed criteria for an optimal bone replacement material [29], which included that "the material should resorb at the same rate that bone is regenerated, with byproducts that are beneficial and easily excreted by the body so that bone will restore to a healthy state". *In-situ* degradation of these materials makes them desirable for clinical applications owing to the release of beneficial ions to the surrounding tissues promoting antibacterial behavior, bone formation and growth, tissue healing, etc. [30–32]. Bioactive glasses have been employed for coating metals [33–35], yet some of these proposed compositions contain aluminum [33,35], which has been associated with defective bone mineralization alongside concerns over its neurotoxicity [36]. Other compositions have been deficient in zinc [34,35], an antibacterial component [32,37,38] to aid in the healing process, also known to inhibit the growth of caries-related bacterial such as *Streptococcus mutans* [39]. Although virtually all materials facilitate biofilm formation which may lead to bacterial infection, bacteria attach less readily to glass [40], providing a rationale for a glass-based solution. As bioactive glasses influence genetic expression, differentiation and cell proliferation by the release of ions [31,41–43], engineering control of the biological response *via* dissolution products creates an opportunity for innovation. The proposed compositions in this work are expected to provide superior performance as they are expected to inhibit bacterial growth due to the addition of zinc, while the absence of aluminum minimizes the possibility of the coating causing toxicity in surrounding tissues. Furthermore, incorporating titanium in the glass compositions is expected enhance osseointegration [10–12].

This study outlines the characterization of two novel bioactive glass series, a silica-based glass series and a borate-based glass series that contain increasing amounts of titanium oxide (TiO_2). Titanium is employed to exploit its osseointegrative capability at the interface of the metallic implant and the bone. TiO_2 will be added in increments of 5 mol% up to 20 mol%. Characterization techniques included energy dispersive spectroscopy (EDS), X-ray diffraction (XRD) differential scanning calorimetry (DSC), Fourier transform infrared (FTIR) spectroscopy, particle size analysis (PSA) and magic-angle spinning-nuclear magnetic resonance (MAS-NMR).

2. Materials and methods

2.1. Glass preparation

Silica-based and borate-based glasses were formulated for this study. The glass compositions, as well as the nomenclature, are reported in Table 1. TiO_2 was added at the expense of SiO_2 for the SRT series and at the expense of B_2O_3 for the BRT series. The glasses were prepared by weighing out appropriate amounts of analytical grade reagents (Fisher Scientific, Ottawa, ON, Canada & Sigma-Aldrich, Oakville, ON, Canada), firing (1400–1500 °C for 1 h for the silica-based glasses, 1200 °C for

Table 1
Glass formulations (mol%).

Reagent	Silica-based glass					Borate-based glasses				
	SRT0	SRT1	SRT2	SRT3	SRT4	BRT0	BRT1	BRT2	BRT3	BRT4
TiO_2	0	5	10	15	20	0	5	10	15	20
SiO_2	52	47	42	37	32	0				
B_2O_3	0					52	47	42	37	32
CaO	12					12				
P_2O_5	6					6				
Na_2O	14					14				
ZnO	16					16				

1 h for borate-based glasses) in silica crucibles, and shock quenching in water. The resulting frit was then ball-milled, and sieved to retrieve glass particulates ≤20 μm.

2.2. Network connectivity (NC)

Network connectivity (NC) provides information on the ability for a glass to degrade and interact with the surrounding tissues [44]. Network connectivity for the proposed formulations was calculated using Eq. (1).

$$NC = \frac{BO - NBO}{NBS} \tag{1}$$

where *BO* is the number of bridging oxygens, *NBO* the number of non-bridging oxygens and *NBS* the total number of bridging species. As network formers, 2 BO are contributed to the glass network per SiO_2 and B_2O_3 in each Q^2 unit; as network modifiers, 2 NBO are contributed per Ca^{2+} and 1 NBO per Na^+. As for P_2O_5, recent work by Hill [45–47] provided insight on the role of phosphates in the glass network, demonstrating its role as an orthophosphate Q^0 (glass modifier) in a SiO_2–P_2O_5–CaO–Na_2O series. Supported by this work, P_2O_5 may only be considered as a glass modifier, with 3 NBO per PO_4^{3-}, and supporting data will be gathered through ^{31}P MAS-NMR. As for ZnO and TiO_2, these reagents behave as network intermediates; therefore, in considering ZnO as a glass former 1 BO is added, and 2 BO are added for TiO_2. Considering these reagents as modifiers, 2 NBO are contributed per Zn^{2+} and per TiO_6^{2-}.

2.3. X-ray diffraction (XRD)

X-ray diffraction (XRD) was performed to confirm that an amorphous state was achieved for all fired materials. Samples were analyzed over the range of $20° \leq 2\theta \leq 80°$, with a step size of 0.05° using a PANalytical X-ray diffractometer (PANalytical, QC, Canada). CuKα (1.54 Å) anode was employed, with a generator voltage of 30 kV and a tube current of 10 mA. Crystalline phases were identified using the International Centre for Diffraction Data (ICDD) standard diffraction patterns.

2.4. Particle size analysis (PSA)

After grinding and sieving of the glass, particle size analysis (PSA) was undertaken to retrieve the average particle size of the glass powder. Particle size analysis was achieved using a BeckmanCoulter Multisizer 4 particle size analyzer (BeckmanCoulter, Fullerton, CA, USA). Three powder samples per glass were evaluated in the range of 2 μm–60 μm. Results were analyzed by Multisizer 4 software, with means and standard deviations based on counting statistics of 30,000 particles per measurement.

Table 2

Network connectivity for the silica-based glasses (left) and for the borate-based glasses (right). FF refers to TiO_2 and ZnO as a glass formers; FM refers to TiO_2 as a glass former and ZnO as a glass modifier; MF refers to TiO_2 as a glass modifier and ZnO as a glass former; and MM refers to TiO_2 and ZnO as glass modifiers.

|	FF	FM	MM	MF		FF	FM	MM	MF
SRT0	2.47	2.04	2.04	2.27	**BRT0**	2.27	2.02	2.02	2.42
SRT1	2.44	2.04	1.62	1.97	**BRT1**	2.27	2.02	1.81	2.27
SRT2	2.41	2.03	1.10	1.62	**BRT2**	2.27	2.02	1.55	2.1
SRT3	2.39	2.03	0.43	1.21	**BRT3**	2.27	2.02	1.22	1.89
SRT4	2.36	2.03	-0.44	0.71	**BRT4**	2.27	2.02	0.78	1.63

2.5. Differential scanning calorimetry (DSC)

A combined differential scanning calorimetry–thermogravimetric analyzer (DSC–TGA) (SDT 2960 Simultaneous DSC–TGA, TA Instruments, DE, USA) was used to measure the glass transition temperature (T_g) and crystallization temperature (T_x) for both glass series. A heating rate of 20 °C min^{-1} was employed using an air atmosphere with alumina in a matched platinum crucible as a reference. Sample measurements were carried out every 6 s between 20 °C and 850 °C.

2.6. Energy dispersive spectroscopy (EDS)

Samples were analyzed using a JEOL JSM-6380LV Scanning Electron Microscopy equipped with an energy-dispersive spectrometer (JEOL, Peabody, MA, USA). Compositional analysis was performed with beam energy of 20.0 keV. EDS results were acquired using Oxford EDS Aztec software, with standard deviations provided by the software based on counting statistics.

2.7. Fourier transform infrared (FTIR) spectroscopy

Silica-based and borate-based ground glass (≤20 μm) was used for this technique in ambient air (23 ± 1 °C). The spectra were collected using a PerkinElmer Spectrum One IR (PerkinElmer, Waltham, MA, USA). Analysis was performed in the wavenumber ranging from 600 cm^{-1} to 4000 cm^{-1} with a spectral resolution of 4 cm^{-1}.
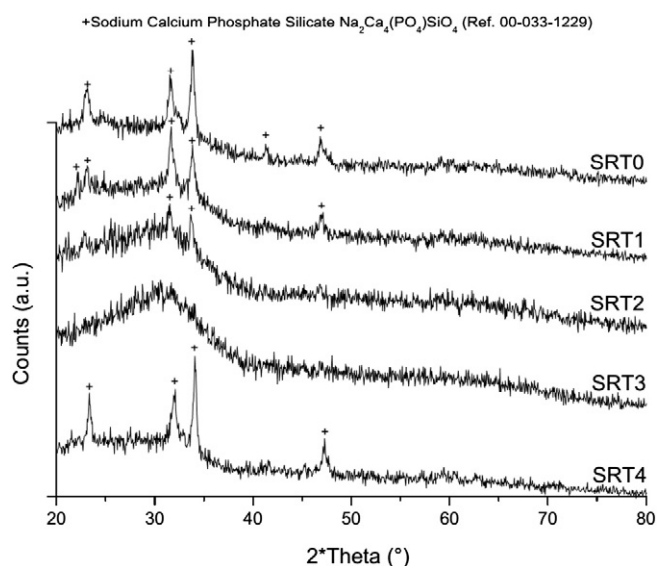
Fig. 1. XRD patterns for silica-based glass series.
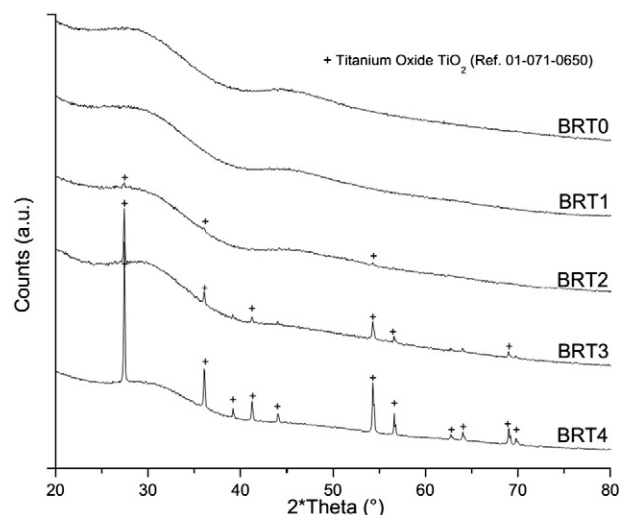
Fig. 2. XRD patterns for borate-based glass series.

2.8. Magic-angle spinning-nuclear magnetic resonance spectroscopy (MAS-NMR)

For the silica-based series, ^{29}Si and ^{31}P MAS-NMR spectra was acquired with high power cw ^{1}H decoupling on a Bruker AVANCE III 200 MHz NMR spectrometer (Bruker Corporation, Billerica, MA, USA) equipped with a 7-mm CPMAS probe. The MAS rate was 4.5 kHz for ^{29}Si and 5 kHz for ^{31}P. The pulse time and recycle delay were 4 μs and 60 s, respectively, for the ^{29}Si MAS-NMR, and 3.25 μs and 60 s, respectively, for the ^{31}P MAS-NMR. For the borate-based series, ^{11}B and ^{31}P MAS-NMR experiments was carried out on an Agilent DD2 500 MHz NMR spectrometer (Agilent Technologies, Inc., Santa Clara, CA, USA) at the magnetic field of 11.7 Tesla. A zirconia rotor with a diameter of 3.2 mm was used for ^{11}B and ^{31}P MAS-NMR measurements. Direct polarization ^{11}B and ^{31}P MAS-NMR spectra was taken at 160.3 MHz and 202.3 MHz, respectively, with 0.725 μs pulse length (π/8-pulse angle) and 5 s recycle delay for ^{11}B MAS-NMR, and with 2.8 μs pulse length (π/2-pulse angle) and 120 s recycle delay for ^{31}P MAS-NMR.

^{29}Si chemical shifts were referenced externally to the –Si(CH$_3$) resonance of tetrakis trimethylsilyl silane $[(CH_3)_3Si]_4Si$, which was assigned a chemical shift of −9.9 ppm with respect to tetramethyl silane $C_4H_{12}Si$ at 0 ppm. ^{31}P chemical shifts were referenced externally to ammonium dihydrogen phosphate $NH_4H_2PO_4$, which was assigned a chemical shift of 0.81 ppm for the silica-based glasses (1.0 ppm for the borate-based

Table 3

Particle size distribution for silica- and borate-based glass series.

	Mean (μm)	S.D. (μm)	d10 (μm)	d50 (μm)	d90 (μm)
SRT0	5.3	4.0	2.1	3.2	9.8
SRT1	3.5	1.7	2.2	3.1	5.7
SRT2	4.8	3.1	2.1	2.7	8.9
SRT3	3.2	1.6	2.1	2.8	4.7
SRT4	3.3	1.6	2.1	2.8	5.1
BRT0	10.1	4.2	6.5	8.6	15.2
BRT1	9.1	3.3	6.4	7.9	13.7
BRT2	9.3	3.4	6.4	8.3	14.5
BRT3	9.7	3.7	6.3	8.5	15.2
BRT4	9.2	3.4	6.3	7.9	14.2

Table 4
DSC results for silica and borate-based glass series.

	$T_g(°C)$	$T_x(°C)$	$\Delta T(°C)$		$T_g(°C)$	$T_x(°C)$	$\Delta T(°C)$
SRT0	619	735	116	BRT0	521	603	82
SRT1	592	670	78	BRT1	530	625	95
SRT2	596	650	54	BRT2	520	670	150
SRT3	610	705	95	BRT3	523	633	110
SRT4	636	710	74	BRT4	528	625	97

glasses) with respect to 85% phosphoric acid H_3PO_4 at 0 ppm. ^{11}B chemical shifts were referenced externally to boric acid H_3BO_3 saturated aqueous solution, which was assigned a chemical shift of -19.49 ppm with respect to boron trifluoride etherate $(C_2H_5)_2O \cdot BF_3$ at 0 ppm.

3. Results

3.1. Network connectivity (NC)

Table 2 lists the network connectivity calculations for the fired glass formulations. For both glass series, the addition of TiO_2 contributing to BO did not alter significantly the network connectivity regardless of ZnO contribution of BO or NBO. In considering the contribution of TiO_2 of NBO in the form of TiO_6^{2-}, network connectivity decreased as TiO_2 is increased, with lower connectivity achieved as ZnO contributed to NBO as network modifier Zn^{2+}.

3.2. X-ray diffraction (XRD)

Crystallinity of the fired glasses was evaluated using XRD. The results are shown in Fig. 1 for the silica-based series and in Fig. 2 for the borate-based series. Results for SRT3 indicate no formation of crystal phases during the firing process; however, SRT0, SRT1, SRT2 and SRT4 exhibit sharp peaks, evidencing crystallinity in these glasses. XRD traces were compared to the ICDD and the phase identified as Sodium Calcium Phosphate Silicate $Na_2Ca_4(PO_4)SiO_4$ (Ref. 00-033-1229) in all cases. In the case of the borate-based series, glasses with up to 5 mol% TiO_2 exhibited no crystal formation; however, at 10 mol% TiO_2 peaks are observed, becoming more pronounced at 15 and 20 mol% TiO_2; partial crystal phase of titanium oxide, TiO_2 (Ref. 01-071-0650) was found in BRT2, BRT3 and BRT4.

3.3. Particle size analysis (PSA)

Upon grinding and sieving each glass the average particle size was assessed using PSA. As observed for the silica-based glass in Table 3, the mean particle size ranges between 3 μm–6 μm. The borate glasses have a mean particle size of around 9 μm.

3.4. Differential scanning calorimetry (DSC)

To determine the transition (T_g) and crystallization (T_x) temperatures for each glass, DSC was employed and results are shown on Table 4. A decrease in T_g for the silica-based glass series occurred with an increase in TiO_2 at the expense of SiO_2 up to 5 mol%. However, further increase in the amount of TiO_2 up to 20 mol% resulted in an increase in T_g. In terms of T_x, increasing TiO_2 from 0 mol% up to 10 mol% translated into a decrease in T_x, with subsequent increase as TiO_2 increased to 20 mol%. For the borate-based glass series, T_g ranged between 520 °C and 530 °C, with no significant changes with the addition of TiO_2. BRT0 (0 mol% TiO_2) exhibited a T_g of 521 °C, reaching a maximum at 5 mol% TiO_2 at 530 °C and a minimum at 10 mol% TiO_2 at 520 °C. T_x was significantly impacted by the addition of TiO_2. Lowest T_x was achieved for control BRT0 at 603 °C, increasing with addition of TiO_2 up to 10 mol% at 670 °C, then steadily decreasing with addition of TiO_2, reaching 625 °C at 20 mol% of TiO_2.

3.5. Energy dispersive spectroscopy (EDS)

Table 5 summarizes the element compositions for the silica- and the borate-based glass series; EDS traces are shown in Fig. 3 for the silica-based series, and in Fig. 4 for the borate-based series. For both series, incorporation of titanium into the materials' structure is confirmed, and a reduction in silica (for the silica-based series), and of boron oxide (for the borate-based series) is observed. Silica was also found in the borate-based glasses, which resulted from using silica crucibles for firing these glasses; however, mole percentage is less than 5.0% (less than 1.5% weight percentage), so its effect may be negligible.

3.6. Fourier transform infra-red (FTIR) spectroscopy

Absorbance spectra for the silica-based and borate-based glass series are shown in Fig. 5 and Fig. 6, respectively. From the absorbance spectra for the silica-based series, three peaks were observed, ~772 cm^{-1},

Table 5
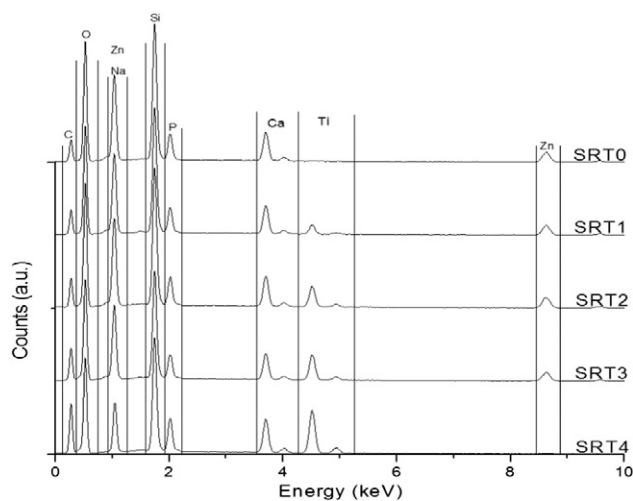Compositional analysis from EDS (mol%). Values in parentheses represent theoretical values.

	Silica-based glass					Borate-based glasses				
Reagent	SRT0	SRT1	SRT2	SRT3	SRT4	BRT0	BRT1	BRT2	BRT3	BRT4
TiO_2	0.0 ±0.0	4.6 ±0.1	9.0 ±0.2	13.4 ±0.2	22.8 ±0.1	0.0 ±0.0	2.7 ±0.1	3.6 ±0.2	7.6 ±0.3	10.7 ±0. 2
	(0)	(5)	(10)	(15)	(20)	(0)	(5)	(10)	(15)	(20)
SiO_2	47.6 ±0.3	43.4 ±0.2	41.6 ±0.4	37.6 ±0.2	37.7 ±0.1	4.2 ±0.2	4.2 ±0.1	2.5 ±0.1	3.3 ±0.2	2.9 ±0.1
	(52)	(47)	(42)	(37)	(32)	(0)	(0)	(0)	(0)	(0)
B_2O_3	0.0 ±0.0	0.0 ±0.0	0.0 ±0.0	0.0 ±0.0	0.0 ±0.0	66.7 ±8.7	60.5 ±8.9	71.5 ±12.2	59.3 ±10.5	53.5 ±6.0
	(0)	(0)	(0)	(0)	(0)	(52)	(47)	(42)	(37)	(32)
CaO	12.1 ±0.1	12.0 ±0.1	11.1 ±0.2	11.0 ±0.3	14.2 ±0.1	6.4 ±0.3	7.0 ±0.3	4.8 ± 0.3	6.2 ±0.2	7.1 ±0.1
	(12)	(12)	(12)	(12)	(12)	(12)	(12)	(12)	(12)	(12)
P_2O_2	5.4 ±0.1	4.8 ±0.1	4.7 ±0.1	4.8 ±0.1	6.1 ±0.1	2.4 ±0.1	3.0 ±0.1	2.2 ±0.1	3.0 ±0.1	3.3 ±0.1
	(6)	(6)	(6)	(6)	(6)	(6)	(6)	(6)	(6)	(6)
Na_2O	18.1 ±0.2	19.2 ±0.2	18.3 ±0.2	18.3 ±0.2	18.5 ±0.1	10.0 ±0.5	12.2 ±0.5	8.7 ±0.3	10.8 ±0.4	12.3 ±0.4
	(14)	(14)	(14)	(14)	(14)	(14)	(14)	(14)	(14)	(14)
ZnO	16.9 ±0.2	16.1 ±0.2	15.3 ± 0.2	14.8 ±0.2	0.7 ±0.1	10.3 ±0.4	10.5 ±0.4	6.6 ±0.2	9.8 ±0.4	10.3 ±0.3
	(16)	(16)	(16)	(16)	(16)	(16)	(16)	(16)	(16)	(16)

Fig. 3. EDS traces for silica-based series.

Fig. 5. FTIR transmittance spectra for silica-based glasses.

~928 cm^{-1} and ~991 cm^{-1}. The 772 cm^{-1} band, belonging to Si–O–Si bending bond [48], remained visible up until the addition of 15 mol% TiO$_2$ (SRT3), fading for 20 mol% TiO$_2$ glass (SRT4), with the 991 cm^{-1} band, belonging to Si–O–Si stretched bond [48], present. This band was also identified for SRT0 and SRT1, and at a lower wavenumber (963 cm^{-1}) for SRT3. Bond Si–O–NBO, centered around 928 cm^{-1} [48], showed no significant shift with the addition of TiO$_2$. A summary of the infrared (IR) assignments is listed in Table 6. For the borate-based series, bands were encountered near 696 cm^{-1}, 770 cm^{-1}, 916 cm^{-1}, 1010 cm^{-1}, 1248 cm^{-1} and 1345 cm^{-1} (refer to Table 6 for the IR assignment). Peaks at 696 cm^{-1} and 770 cm^{-1} indicate the presence of B–O–B bending bond [49], with absorbance intensity decreasing consistently decreasing with the additional of TiO$_2$. The peak at 916 cm^{-1}, belonging to stretching bond B–O in diborate groups [49], maintained absorbance levels with the increase in the content of TiO$_2$, with slight shifts for BRT1 and BRT2, and significant shifts for BRT3 (to 859 cm^{-1}) and BRT4 (to 900 cm^{-1}), compositions which exhibited the crystallization of TiO$_2$.

3.7. Magic-angle spinning-nuclear magnetic resonance spectroscopy (MAS-NMR)

^{29}Si and ^{31}P NMR spectra for the silica-based series are shown in Figs. 7 and 8, respectively; ^{11}B and ^{31}P NMR spectra for the borate-based glass series are shown in Figs. 9 and 10, respectively. A consistent
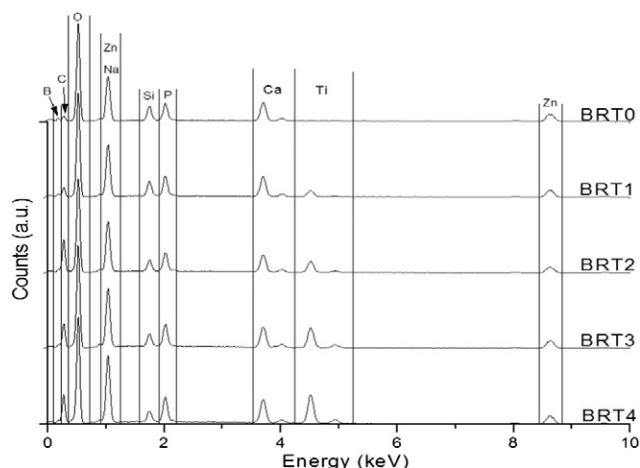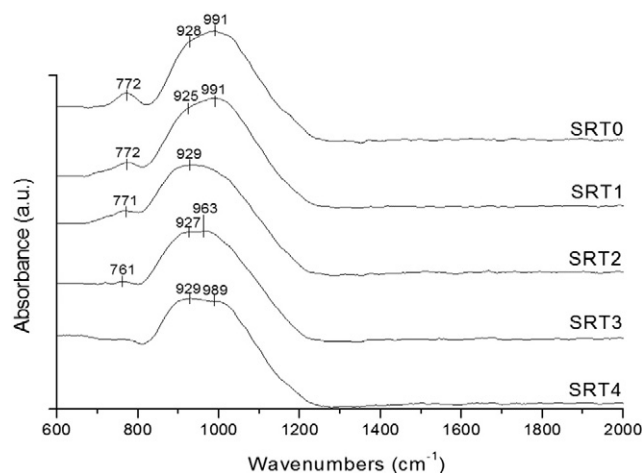
increase in chemical shift for ^{29}Si, from -93.67 ppm (Q^4) [50] at 0 mol% TiO$_2$, is observed with the addition of TiO$_2$ up to 15 mol% TiO$_2$, with a significant decrease at 20 mol%. Two peaks, ~4.26 ppm and ~2.60 ppm (Q^0 and Q^1, respectively) [50], are observed in the ^{31}P spectra for the silica-based glass series for TiO$_2$ content at 0, 5 and 20 mol%, whereas a single peak is observed at 10 and 15 mol%. ^{11}B NMR exhibited three peaks, ~13.61 ppm, ~8.93 ppm and ~0.43 ppm, corresponding to Q^3 structures in the form of symmetric BO$_3$, asymmetric BO$_3$, and Q^4 structures in the form of BO$_4$ species, respectively [51], with chemical shifts increasing with the addition of TiO$_2$ up to 10 mol%, with BRT2 peaking at ~14.05 ppm, ~9.51 ppm and ~0.87 ppm, respectively; however, further addition of TiO$_2$ and the presence of crystal phase TiO$_2$ resulted in a decrease in chemical shift to ~13.76 ppm, ~9.07 ppm and ~0.58 ppm, respectively, at 15 mol%. At 20 mol%, and with greater crystallinity intensities, the chemical shift shifted to ~14.05 ppm, ~9.51 ppm and ~0.73 ppm. For the borate-based glass series, the ^{31}P NMR spectra exhibits a single peak, ~4.82 ppm (Q^0) [50], for all compositions, with the chemical at the peak decreasing with the addition of TiO$_2$ from 0 to 10 mol%, then increasing at 15 and 20 mol%.

4. Discussion

With respect to the silica-based series, amorphous glasses were achieved for glass SRT3, which contains 15 mol% of TiO$_2$, evidenced by the amorphous hump found in the XRD traces; whereas partial crystallinity (i.e. the amorphous hump remained visible in the background of the XRD traces, as exhibited by SRT3) was found for glasses SRT0,
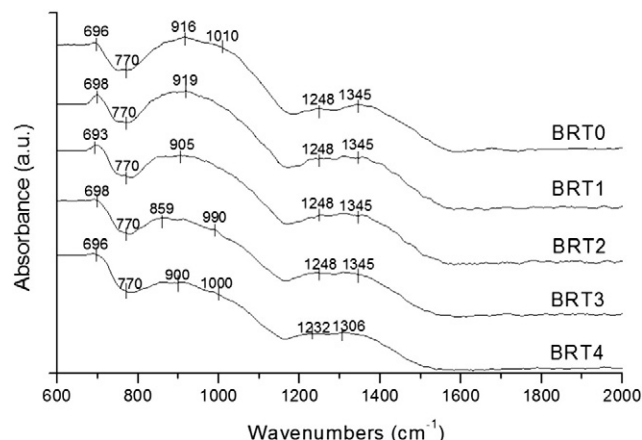

Fig. 4. EDS traces for borate-based series.

Fig. 6. FTIR transmittance spectra for borate-based glasses.

Table 6
Infrared (IR) peak assignment for silica-based and borate-based glass spectra.

Wavenumber (cm⁻¹)	IR Assignment	Reference
~771	Si–O–Si bond-bending	[48]
~928	Si–O–NBO	
~991	Si–O–Si bond-stretching	
~696, ~770	B–O–B bond-bending vibrations	[49] Ø represents oxygen atom bridging two boron atoms.
~916	B–O bond-stretching vibrations in BO_4 units from diborate groups	
~1010	B–Ø bond-stretching vibrations of $BØ_4^-$ tetrahedra from tri-, tetra- and pentaborate groups	
~1248	Asymmetric stretching vibration of B–O bonds from orthoborate groups	
~1345	Asymmetric stretching modes of borate triangles $BØ_3$ and $BØ_2O–NBO$	

SRT1, SRT2 and SRT4, containing 0 mol%, 5 mol%, 10 mol% and 20 mol% TiO_2, respectively. XRD traces were compared to the ICDD database, and identified as Sodium Calcium Phosphate Silicate $Na_2Ca_4(PO_4)SiO_4$ (Ref. 00-033-1229) in all cases. ^{31}P NMR for the partially crystallized glasses exhibited two peaks (~4.26 ppm and ~2.60 ppm), with the exception of SRT2, which may be attributed to low intensity crystal peaks compared to SRT0, SRT1 and SRT4; amorphous glass SRT3 presented only one peak (~4.71 ppm). The presence of the Sodium Calcium Phosphate Silicate phase may explain the occurrence on the second peak (~2.60 ppm) for the crystalline materials, accounting for Q^1 tetrahedron (pyrophosphate) in $Na_2Ca_4(PO_4)SiO_4$, whereas the peak ~4.26 ppm and ~4.71 ppm indicates the presence of orthophosphate (Q^0 tetrahedron) [50], supporting the statement that P_2O_5 would enter the glass network as a network modifier, rather than as a network former [46]. ^{29}Si NMR peak was located at −93.67 ppm for SRT0 (Q^4), increasing as TiO_2 is added up to 15 mol% to −90.44 ppm, then decreasing to −96.90 ppm for SRT4 at 20 mol%. Considering the crystal peak intensities, the decreased chemical shift in ^{29}Si is observed with increased intensity, suggesting that phase $Na_2Ca_4(PO_4)SiO_4$ promoted the formation of Q^4 structures in the glasses.

As for the borate-based series, no crystallization occurred in glasses with up to 10 mol% TiO_2, i.e. BRT0 and BRT1. Partial crystal phase of titanium oxide TiO_2 (Ref. 01-071-0650) was found in BRT2, BRT3 and BRT4, indicating a possible saturation point for the addition of TiO_2 to the control glass BRT0. Studies have been performed to determine the effect of crystallinity on glass solubility and ion release [52], which points towards amorphous materials providing better solubility and ion release profiles compared against the homologous crystalline materials. As coating materials, degradation behavior of these glasses is important
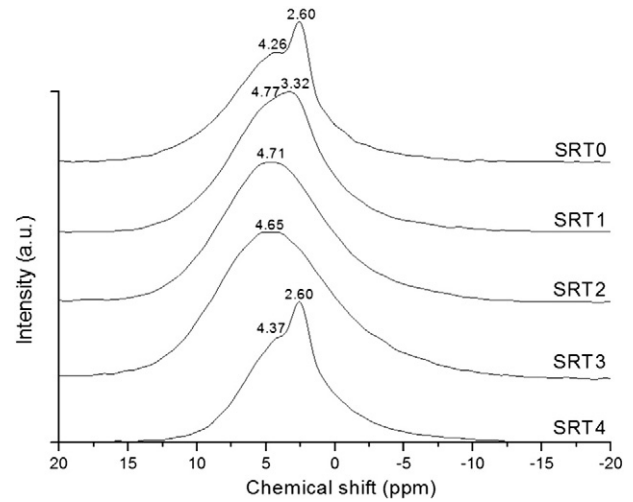

Fig. 8. ^{31}P chemical shift for the silica-based glass series.

to bacterial inhibition and osseointegration promotion; therefore, further studies on the degradation of these partially crystallized materials would confirm how effective these materials are in releasing ions into the body and would help quantify the effect of partial crystallinity for these formulations. Comparing to the SRT results, ^{31}P for the BRT series presented only one peak for all glasses, centered at 4.82 ppm for BRT0, corresponding to orthophosphate PO_4^{-3} (Q^0 tetrahedron) [50], decreasing with the addition of TiO_2 up to 10 mol%, with BRT2 exhibiting a peak at 2.71 ppm; however, the presence of crystallinity translated into an increase to 2.74 ppm for BRT3, and further to 3.12 ppm for BRT4, correlating the increase in chemical shift with the increase in crystallinity intensity. ^{11}B NMR exhibited three peaks, ~13.61 ppm, ~8.93 ppm and ~0.43 ppm, corresponding to Q^3 structures in the form of symmetric BO_3, asymmetric BO_3, and Q^4 structures in the form of BO_4 species, respectively [51]; furthermore, it was observed from FTIR the presence of different boron-to-oxygen bonds, as shown in Table 6. It may be argued that the presence of TiO_2 crystals perturbed stretching bond B–O in diborate groups, but favoring these bonds for tri-, tetra- and pentaborate groups, as the peak at 1010 cm⁻¹ is only observed for the control BRT0, then also in BRT3 and BRT4, with minor shifts to 990 cm⁻¹ and 1000 cm⁻¹, respectively. The maxima around
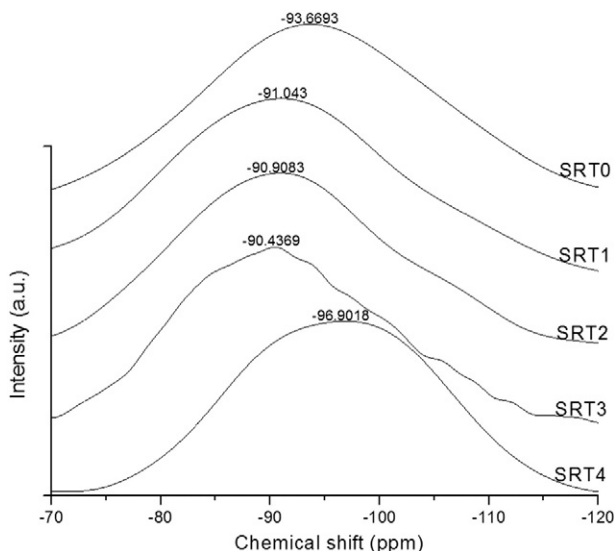

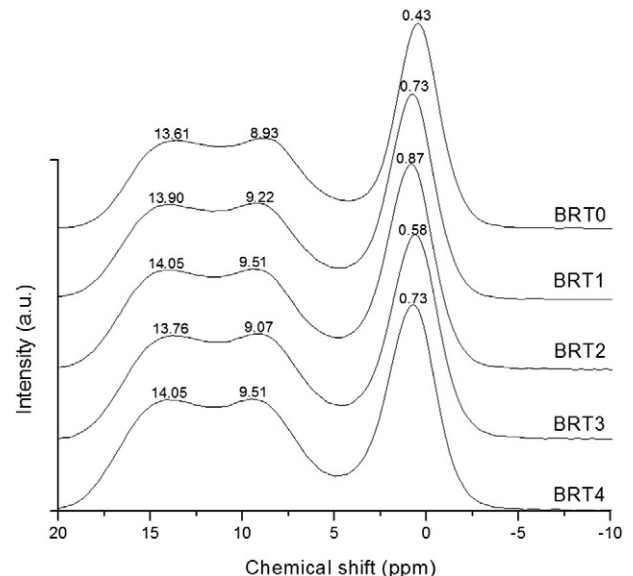**Fig. 7.** ^{29}Si chemical shift for the silica-based glass series.

Fig. 9. ^{11}B chemical shift for the borate-based glass series.
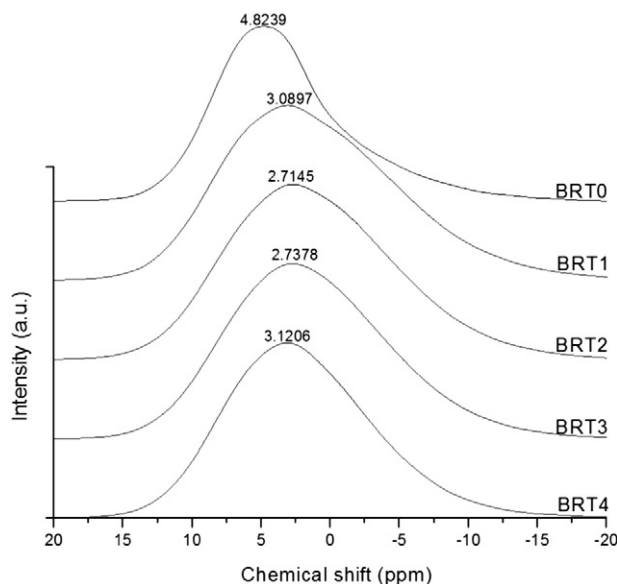
Fig. 10. ^{31}P chemical shift for the borate-based glass series.

1248 cm^{-1} and 1345 cm^{-1}, belonging to asymmetric stretching of B–O bonds, remained unchanged up until 15 mol% TiO$_2$, but experienced a shift to 1232 cm^{-1} and 1306 cm^{-1} for BRT4, respectively, which may be attributed to the presence of crystal phase TiO$_2$ at higher concentration compared to BRT3. Provided the absence of IR peaks pertaining to bonds of titanium, it suggests TiO$_2$ behavior as a network modifier, rather than a network former, for both silica-based and borate-based glasses.

It was found that as TiO$_6^{2-}$ enter the glass network for the proposed materials, a decrease of NC below 2 is expected, which by definition favors bioactivity, with Zn^{+2} contributing as well to the decrease in NC. NBO disrupt the glass network by depolymerizing Si–O–Si and B–O–B [53,54], which facilities ion release from the glass network, increasing bioactivity [55], suggesting that TiO$_2$ entering the glass network as modifier TiO$_6^{2-}$, rather than as a former, allows for better bioactivity.

In treating the bioactive glasses for coating, the processing window (ΔT) is defined by the range between T$_x$ and T$_g$; a larger processing window is more desirable as it allows for a wider range of temperatures in which to process the glass [56]. The smallest processing window, 54 °C, occurred for SRT2, making is less suitable for processing in terms of processing window, whereas the maximum processing window, 116 °C, occurred for SRT0. Greater processing windows were found for the BRT series, with the smallest one (BRT0) at 82 °C and the largest one (BRT2) at 150 °C. Crystallization temperatures for both glass series are, however, below the β transus temperature for commercially pure (cp) Ti (882 $\pm$ 2 °C) and Ti6Al4V (995 °C to 1010 °C) [57], two preferred metals for implant applications; therefore, in coating titanium with these glasses, no α to β transformation will occur, preserving the oxidation resistance in alpha phases compared to beta phases. With the increase in TiO$_2$ in the silica-based series, a decrease was observed in the processing window ΔT up to 10 mol%, with an increase with further increase in TiO$_2$. Increasing TiO$_2$ beyond 10 mol% directly translated into an increase in T$_g$ and T$_x$, with the absence of crystal peaks in SRT3 resulting in a greater ΔT, attributed to higher energy required to promote the formation of new crystal structures within the glassy material, thus increasing T$_g$. For the borate-based series, at 10 mol% maximum T$_x$ was achieved, where low crystal peak intensities are first encountered for this series; the addition of TiO$_2$ beyond this point increased peak intensities, which translated into decreased T$_x$ (and subsequently ΔT). It may be suggested that the presence of crystal phase TiO$_2$ favored crystallization, hence reducing T$_x$ as TiO$_2$ was increased beyond 10 mol% in the borate-based series.

5. Conclusions

Incorporation of TiO$_2$ to silica-based and borate-based glasses was achieved through a standard glass-firing process and characterization techniques were employed to evaluate the intrinsic features of these glasses. MAS-NMR proved the role of P$_2$O$_5$ as a network modifier for both glass series by evidencing only Q^0 structures (and Q^1 structures for the silica-based glasses with crystal structures), whereas FTIR proved the role of TiO$_2$ as a network modifier by lack of peaks assignable to titanium bonding. Upon characterization, the two glass series are expected to have potential as metal coatings owing to the favorable network connectivity calculations, suggesting the glasses will degrade *in-situ* and release ions at the site of implantation. Additionally, thermal behavior of these glasses provided for processing windows which make them suitable for enameling metallic implants, with the borate-based series exhibiting greater processing windows over the silica-based series. Moreover, further studies will provide additional insight on the advantages and disadvantages of employing borate-based glasses for coating applications in contrast to silica-based glasses, expanding the range of applications of bioactive materials.

Acknowledgments

References

[1] M. Pitkin, Design features of implants for direct skeletal attachment of limb prostheses, J. Biomed. Mater. Res. A 101 (11) (2013) 3339–3348.
[2] K. Hagberg, E. Haggstrom, M. Uden, R. Branemark, Socket versus bone-anchored trans-femoral prostheses: hip range of motion and sitting comfort, Prosthetics Orthot. Int. 29 (2) (2005) 153–163.
[3] D.G. Shurr, J.W. Michael, T.M. Cook, Prosthetics and Orthotics, Prentice Hall, East Norwalk, 2002.
[4] J. Hughes, Biomechanics of the through-knee prosthesis, Prosthetics Orthot. Int. 7 (2) (1983) 96–99.
[5] M. Zhang, C. Roberts, Comparison of computational analysis with clinical measurement of stresses on below-knee residual limb in a prosthetic socket, Med. Eng. Phys. 22 (9) (2000) 607–612.
[6] M. Tanaka, Y. Akazawa, A. Nakagawa, I. Kitayama, Identification of pressure distribution at the socket interface of an above-knee prosthesis, Adv. Eng. Softw. 28 (6) (1997) 379–384.
[7] C.M. Schuch, C.H. Pritham, Current transfemoral sockets, Clin. Orthop. Relat. Res. 361 (1999) 48–54.
[8] L.A. Frossard, R. Tranberg, E. Haggstrom, M. Pearcy, R. Branemark, Load on osseointegrated fixation of a transfemoral amputee during a fall: loading, descent, impact and recovery analysis, Prosthetics Orthot. Int. 34 (1) (2010) 85–97.
[9] C.J. Pendegrass, A.E. Goodship, G.W. Blunn, Development of a soft tissue seal around bone-anchored transcutaneous amputation prostheses, Biomaterials 27 (23) (2006) 4183–4191.
[10] R. Branemark, P.I. Branemark, B. Rydevik, R.R. Myers, Osseointegration in skeletal reconstruction and rehabilitation: a review, J. Rehabil. Res. Dev. 38 (2) (2001) 175–182.
[11] P.I. Branemark, B.O. Hansson, R. Adell, U. Breine, J. Lindstrom, O. Hallen, A. Ohman, Osseointegrated implants in the treatment of the edentulous jaw, Scand. J. Plast. Reconstr. Surg. 11 (1997) 1–52.
[12] P.I. Branemark, Osseointegration and its experimental background, J. Prosthet. Dent. 50 (3) (1983) 399–410.
[13] J.B. Webster, T. Chou, M. Kenly, M. English, T.L. Roberts, R.D. Bloebaum, Perceptions and acceptance of osseointegration among individuals with lower limb amputations: a prospective survey study, J. Prosthet. Orthot. 21 (4) (2009) 215–222.
[14] J. Sullivan, M. Uden, K.P. Robinson, S. Sooriakumaran, Rehabilitation of the trans–femoral amputee with an osseointegrated prosthesis: the United Kingdom experience, Prosthetics Orthot. Int. 27 (2) (2003) 114–120.
[15] J. Tillander, K. Hagberg, L. Hagberg, R. Branemark, Osseointegrated titanium implants for limb prostheses attachments: infectious complications, Clin. Orthop. Relat. Res. 468 (10) (2010) 2781–2788.

[16] K.A. Drygas, R. Taylor, C.G. Sidebotham, R.R. Hugate, H. McAlexander, Transcutaneous tibial implants: a surgical procedure for restoring ambulation after amputation of the distal aspect of the tibia in a dog, Vet. Surg. 37 (4) (2008) 322–327.

[17] B.J. Farrell, B.I. Prilutsky, R.S. Kistenberg, J.F. Dalton, M. Pitkin, An animal model to evaluate skin–implant–bone integration and gait with a prosthesis directly attached to the residual limb, Clin. Biomech. 29 (3) (2014) 336–349.

[18] R. Ghosh, S. Gupta, Bone remodelling around cementless composite acetabular components: the effects of implant geometry and implant–bone interfacial conditions, J. Mech. Behav. Biomed. Mater. 32 (2014) 257–269.

[19] A. Chaudhari, A. Braem, J. Vleugels, J.A. Martens, I. Naert, M.V. Cardoso, J. Duyck, Bone tissue response to porous and functionalized titanium and silica based coatings, PLoS One 6 (9) (2011) e24186.

[20] P.R. Klokkevold, R.D. Nishimura, M. Adachi, A. Caputo, Osseointegration enhanced by chemical etching of the titanium surface. A torque removal study in the rabbit, Clin. Oral Implants Res. 8 (6) (1997) 442–447.

[21] D. Buser, R.K. Schenk, S. Steinemann, J.P. Fiorellini, C.H. Fox, H. Stich, Influence of surface characteristics on bone integration of titanium implants. A histomorphometric study in miniature pigs, J. Biomed. Mater. Res. 25 (7) (1991) 889–902.

[22] R.J. Furlong, J.F. Osborn, Fixation of hip prostheses by hydroxyapatite ceramic coatings, J. Bone Joint Surg. Br. Vol. 73 (5) (1991) 741–745.

[23] L.I. Havelin, L.B. Engesæter, B. Espehaug, O. Furnes, S.A. Lie, S.E. Vollset, The Norwegian arthroplasty register: 11 years and 73,000 arthroplasties, Acta Orthop. 71 (4) (2000) 337–353.

[24] R.G. Geesink, Osteoconductive coatings for total joint arthroplasty, Clin. Orthop. Relat. Res. 395 (2002) 53–65.

[25] C. Logghe, C.H. Van Ossel, W. D'Hoore, H. Ezzedine, G. Wauters, J.J. Haxhe, Evaluation of chlorhexidine and silver-sulfadiazine impregnated central venous catheters for the prevention of bloodstream infection in leukaemic patients: a randomized controlled trial, J. Hosp. Infect. 37 (2) (1997) 145–156.

[26] B. Gottenbos, H.C. van der Mei, F. Klatter, P. Nieuwenhuis, H.J. Busscher, In vitro and in vivo antimicrobial activity of covalently coupled quaternary ammonium silane coatings on silicone rubber, Biomaterials 23 (6) (2002) 1417–1423.

[27] L.L. Hench, R.J. Splinter, W.C. Allen, T.K. Greenlee, Bonding mechanisms at the interface of ceramic prosthetic materials, J. Biomed. Mater. Res. 5 (6) (1971) 117–141.

[28] W. Cao, L.L. Hench, Bioactive materials, Ceram. Int. 22 (6) (1996) 493–507.

[29] J.R. Jones, L.M. Ehrenfried, L.L. Hench, Optimising bioactive glass scaffolds for bone tissue engineering, Biomaterials 27 (7) (2006) 964–973.

[30] G. Kaur, O.P. Pandey, K. Singh, D. Homa, B. Scott, G. Pickrell, A review of bioactive glasses: their structure, properties, fabrication and apatite formation, J. Biomed. Mater. Res. A 102 (1) (2014) 254–274.

[31] I.D. Xynos, A.J. Edgar, L.D. Buttery, L.L. Hench, J.M. Polak, Ionic products of bioactive glass dissolution increase proliferation of human osteoblasts and induce insulin-like growth factor II mRNA expression and protein synthesis, Biochem. Biophys. Res. Commun. 276 (2) (2000) 461–465.

[32] D. Boyd, H. Li, D.A. Tanner, M.R. Towler, J.G. Wall, The antibacterial effects of zinc ion migration from zinc-based glass polyalkenoate cements, J. Mater. Sci. Mater. Med. 17 (6) (2006) 489–494.

[33] M. Chen, W. Li, M. Shen, S. Zhu, F. Wang, Glass coatings on stainless steels for high-temperature oxidation protection: echanisms, Corros. Sci. 82 (2014) 316–327.

[34] A. Sola, D. Bellucci, V. Cannillo, Enamelled coatings produced with low-alkaline bioactive glasses, Surf. Coat. Technol. 248 (2014) 1–8.

[35] L. Peddi, R.K. Brow, R.F. Brown, Bioactive borate glass coatings for titanium alloys, J. Mater. Sci. Mater. Med. 19 (9) (2008) 3145–3152.

[36] T.P. Flaten, A.C. Alfrey, J.D. Birchall, J. Savory, R.A. Yokel, Status and future concerns of clinical and environmental aluminum toxicology, J. Toxic. Environ. Health A 48 (6) (1996) 527–542.

[37] A. Coughlan, K. Scanlon, B.P. Mahon, M.R. Towler, Zinc and silver glass polyalkenoate cements: An evaluation of their antibacterial nature, Bio-Med. Mater. Eng. 20 (2) (2010) 99–106.

[38] S. Murphy, A.W. Wren, M.R. Towler, D. Boyd, The effect of ionic dissolution products of Ca–Sr–Na–Zn–Si bioactive glass on in vitro cytocompatibility, J. Mater. Sci. Mater. Med. 21 (10) (2010) 2827–2834.

[39] J. Foley, A. Blackwell, Ion release from copper phosphate cement and influence on *Streptococcus mutans* growth in vitro: a comparative study, Caries Res. 37 (6) (2002) 416–424.

[40] R.M. Donlan, Biofilms: microbial life on surfaces, Emerg. Infect. Dis. J. 8 (9) (2002) 881–890.

[41] I.D. Xynos, M.V.J. Hukkanen, J.J. Batten, L.D. Buttery, L.L. Hench, J.M. Polak, Bioglass® 45S5 stimulates osteoblast turnover and enhances bone formation in vitro: implications and applications for bone tissue engineering, Calcif. Tissue Int. 67 (4) (2000) 321–329.

[42] I.D. Xynos, A.J. Edgar, L.D. Buttery, L.L. Hench, J.M. Polak, Gene-expression profiling of human osteoblasts following treatment with the ionic products of Bioglass® 45S5 dissolution, J. Biomed. Mater. Res. 55 (2) (2001) 151–157.

[43] A. Asselin, S. Hattar, M. Oboeuf, D. Greenspan, A. Berdal, J.M. Sautier, The modulation of tissue-specific gene expression in rat nasal chondrocyte cultures by bioactive glasses, Biomaterials 25 (25) (2004) 5621–5630.

[44] R. Hill, An alternative view of the degradation of bioglass, J. Mater. Sci. Lett. 15 (13) (1996) 1122–1125.

[45] R.G. Hill, D.S. Brauer, Predicting the bioactivity of glasses using the network connectivity or split network models, J. Non-Cryst. Solids 357 (24) (2011) 3884–3887.

[46] M.D. O'Donnell, S.J. Watts, R.V. Law, R.G. Hill, Effect of P_2O_5 content in two series of soda lime phosphosilicate glasses on structure and properties–part I: NMR, J. Non-Cryst. Solids 354 (30) (2008) 3554–3560.

[47] D.S. Brauer, N. Karpukhina, R.V. Law, R.G. Hill, Structure of fluoride-containing bioactive glasses, J. Mater. Chem. 19 (31) (2009) 5629–5636.

[48] J. Serra, P. González, S. Liste, C. Serra, S. Chiussi, B. León, M. Pérez-Amor, H.O. Ylänen, M. Hupa, FTIR and XPS studies of bioactive silica based glasses, J. Non-Cryst. Solids 332 (1) (2003) 20–27.

[49] R. Ciceo-Lucacel, I. Ardelean, FT-IR and Raman study of silver lead borate-based glasses, J. Non-Cryst. Solids 353 (18) (2007) 2020–2024.

[50] A. Pedone, T. Charpentier, M.C. Menziani, The structure of fluoride-containing bioactive glasses: new insights from first-principles calculations and solid state NMR spectroscopy, J. Mater. Chem. 22 (25) (2012) 12599–12608.

[51] J.F. Stebbins, P. Zhao, S. Kroeker, Non-bridging oxygens in borate glasses: characterization by ^{11}B and ^{17}O MAS and 3QMAS NMR, Solid State Nucl. Magn. Reson. 16 (1) (2000) 9–19.

[52] Y. Li, A. Coughlan, F.R. Laffir, D. Pradhan, N.P. Mellott, A.W. Wren, Investigating the mechanical durability of bioactive glasses as a function of structure, solubility and incubation time, J. Non-Cryst. Solids 380 (2013) 25–34.

[53] A.W. Wren, F.R. Laffir, A. Kidari, M.R. Towler, The structural role of titanium in Ca–Sr–Zn–Si/Ti glasses for medical applications, J. Non-Cryst. Solids 357 (3) (2011) 1021–1026.

[54] E.I. Kamitsos, G.D. Chryssikos, Borate glass structure by Raman and infrared spectroscopies, J. Mol. Struct. 247 (1991) 1–16.

[55] J. Serra, P. Gonzalez, S. Liste, S. Chiussi, B. Leon, M. Pérez-Amor, H.O. Ylänen, M. Hupa, Influence of the non-bridging oxygen groups on the bioactivity of silicate glasses, J. Mater. Sci. Mater. Med. 13 (12) (2002) 1221–1225.

[56] N. Lotfibakhshaiesh, D.S. Brauer, R.G. Hill, Bioactive glass engineered coatings for Ti6Al4V alloys: influence of strontium substitution for calcium on sintering behaviour, J. Non-Cryst. Solids 356 (44) (2010) 2583–2590.

[57] G. Welsch, R. Boyer, E.W. Collings (Eds.), Materials Properties Handbook: Titanium Alloys, ASM international, Materials Park, 1993.